Journal of Materials Chemistry A

Tuning the Co/Fe ratio in BaCoxFe0.8-xZr0.1Y0.1O3-δ, a promising triple ionic and electronic conducting oxide, to boost electrolysis and fuel cell performance

Journal:	*Journal of Materials Chemistry A*
Manuscript ID	TA-ART-04-2022-003150.R1
Article Type:	Paper
Date Submitted by the Author:	24-Oct-2022

Complete List of Authors:	Shin, Yewon; Colorado School of Mines, Dept of Metallurgical and Materials Engineering Kim, You-dong; Colorado School of Mines, Dept of Metallurgical and Materials Engineering Sanders, Michael; Colorado School of Mines Harvey, Steven; National Renewable Energy Laboratory Walker, Michael; Colorado School of Mines, Dept of Metallurgical and Materials Engineering O'Hayre, Ryan; Colorado School of Mines, Dept of Metallurgical and Materials Engineering

Received 00th January 20xx,

Accepted 00th January 20xx

DOI: 10.1039/x0xx00000x

Tuning the Co/Fe ratio in $BaCo_xFe_{0.8-x}Zr_{0.1}Y_{0.1}O_{3-\delta}$, a promising triple ionic and electronic conducting oxide, to boost electrolysis and fuel cell performance

Yewon Shin,*[a] You-dong Kim,[a] Michael Sanders,[a] Steven P. Harvey,[b] Michael Walker,[a] and Ryan O'Hayre[a]

The triple conducting oxide $BaCo_{0.4}Fe_{0.4}Zr_{0.1}Y_{0.1}O_{3-\delta}$ (BCFZY4411), which accommodates simultaneous transport of protons, oxygen ions, and p-type electronic carriers, has been intensively investigated in recent years as a high-performance positive electrode material for fuel cell and electrolysis applications. The heavy Co and Fe-based transition metal doping in BCFZY4411 ensures adequate electrical conductivity while the multiple oxidation states of Co and Fe assist the electrocatalytic and redox ability. Despite the considerable role of Co and Fe transition metal doping in controlling electrochemical activity, however, the study of alternative BCFZY compositions with varying Co/Fe ratios has not yet been pursued. Here, we evaluate the electrochemical performance of a series of $BaCo_xFe_{0.8-x}Zr_{0.1}Y_{0.1}O_{3-\delta}$ compositions with varying Co/Fe ratio (x = 0.1, 0.2, 0.4, 0.6, 0.7) and use oxygen ion tracer diffusion and in-situ high-temperature X-ray diffraction to investigate the effect of Co/Fe ratio on electrocatalytic activity, electronic conductivity, oxygen ion incorporation and transport kinetics, and thermomechanical behavior. We find that Co-rich BCFZY7111 yields the highest performance due to exceptionally high oxygen vacancy diffusion and shows a lower and more linear thermal expansion behavior compared to Fe-rich compositions. A protonic ceramic button cell incorporating a BCFZY7111 positive electrode yields a peak power density of 695 mW·cm^{-2} under fuel cell mode and an electrolysis current density of 1976 mA·cm^{-2} at 1.4 V at 600 °C, underscoring the promise of this new BCFZY electrode composition.

1. Introduction

Triple conducting oxides (TCOs), which accommodate the simultaneous transport of protons, oxygen ions, and electronic charge carriers, are emerging as particularly attractive candidates for a variety of low temperature (e.g., alkaline) and high temperature (e.g., ceramic) fuel cell and electrolysis applications.[1–3] TCOs have been introduced in recent years to overcome the barriers presented by previous single-ion conducting mixed ionic-electronic conducting (MIEC) electrode materials. TCOs have garnered particular attention for use as protonic ceramic fuel cell (PCFC) cathodes, although they have also shown exceptional performance when used in more conventional oxygen-ion conducting solid oxide fuel cells (SOFCs)[4–8] and even low-temperature alkaline fuel cells.[9] The simultaneous accommodation of three charge carriers (generally $H^+/h^+/O^{2-}$) in a TCO expands the electrochemically active region to the entire surface area of the cathode, thereby eliminating reaction restrictions associated with triple-phase boundary sites. Widely investigated TCO materials include $BaCo_{0.4}Fe_{0.4}Zr_{0.1}Y_{0.1}O_{3-\delta}$ (BCFZY4411), $PrBa_{0.5}Sr_{0.5}Co_{1.5}Fe_{0.5}O_{5+\delta}$ (PBSCF), and $BaGd_{0.8}La_{0.2}Co_2O_{6-\delta}$ (BGLC).[10–12]

BCFZY4411 is particularly well studied due to its high electrochemical activity, stable cubic perovskite crystal structure, good compatibility with many electrolyte materials, earth-abundant composition, and facile synthesis. The low-activation energy for proton migration in BCFZY4411 enables a decrease in the operating temperature of ceramic electrochemical devices while heavy transition metal doping ensures adequate electrical conductivity and electrochemical reactivity. Moreover, the multiple oxidation states of Co and Fe assist the electrocatalytic and redox ability of BCFZY4411 while Zr and Y provide structural and chemical stability. Recent investigations have aimed to slightly modify the composition of BCFZY4411 to obtain optimal oxygen reduction reaction (ORR) activity. Wang et al. and Ren et al. both reported that BCFZY4411 with 10% A-site deficiency (i.e., $Ba_{0.9}Co_{0.4}Fe_{0.4}Zr_{0.1}Y_{0.1}O_{3-\delta}$, or B0.9CFZY), showed enhanced ORR activity with lower cathode area specific resistance (ASR) than stochiometric BCFZY4411.[13,14] Similarly, B-site deficient BCFZY4411, $Ba(Co_{0.4}Fe_{0.4}Zr_{0.1}Y_{0.1})_{0.95}O_{3-\delta}$ (BCFZY-0.95), has shown decreased ASR and increased ORR performance compared to stochiometric BCFZY4411.[15,16] These studies demonstrate that the BCFZY system shows remarkable compositional versatility and tolerance to non-stoichiometry, and that slight A or B-site deficiency can even boost performance. Researchers have also explored changes to the B-site cation composition. Duffy et al. modified the Zr/Y ratio and

a. Department of Metallurgical and Materials Engineering, Colorado School of Mines, 1500 Illinois St., Golden, CO, 80401, USA
b. National Renewable Energy Laboratory, 15013 Denver West Parkway, Golden, CO, 80401, USA

†Electronic Supplementary Information (ESI) available: Additional experimental details for sample preparations, oxygen ion tracer diffusion parameters for various BCFZY compositions, calculated total and chemical expansion by in-situ high temperature XRD (HT-XRD), FE-SEM image of cathode morphology, XRD patterns, and tables for obtained unit cell parameter by in-situ HT XRD and oxygen ion tracer diffusion parameters of BCFZY compositions at 400 – 700 °C. See DOI: 10.1039/x0xx00000x

assessed the surface exchange rates using the electrical conductivity relaxation (ECR) method.[17] Papac et al. also studied compositional variations in pulse-laser deposited (PLD) combinatorial thin-film BCFZY libraries by electrochemical impedance spectroscopy (EIS) and identified some promising candidates to be characterized further, although direct electrochemical validation of alternative compositions via symmetric or full-cell testing was not pursued.[18]

The heavy transition metal Co and Fe doping in BCFZY is central to determining its electronic conductivity, oxygen vacancy content, and electrochemical activity. However, a detailed study of alternative BCFZY compositions by varying the Co/Fe ratio has not yet been pursued. Prior studies from other mixed-conducting perovskite electrodes such as $La_xSr_{1-x}Co_yFe_{1-y}O_{3-\delta}$ (LSCF) and $Ba_xSr_{1-x}Co_yFe_{1-y}O_{3-\delta}$ (BSCF) indicate that Co and Fe can have differing effects on redox activity, oxygen vacancy content/mobility, and electronic conductivity,[6,19,20] thus it is likely that the electrochemical performance of BCFZY can be further optimized by tailoring the Co/Fe ratio. Given this motivation, here we investigate a series of $BaCo_xFe_{0.8-x}Zr_{0.1}Y_{0.1}O_{3-\delta}$ compositions ($0.1 \le x \le 0.7$) via oxygen tracer diffusion, DC conductivity, and in-situ high-temperature X-ray diffraction (HT-XRD) experiments coupled to symmetric and full cell performance studies to elucidate how the Co/Fe ratio affects electronic conductivity, oxygen ion incorporation and transport kinetics, thermomechanical behavior, and overall electrochemical performance. Our results show that increasing the Co/Fe ratio may provide the opportunity to simultaneously increase electrochemical performance and electronic conductivity as well as thermomechanical compatibility with common ceramic electrolyte materials.

2. Experimental Section

2.1 Synthesis of $BaCo_xFe_{0.8-x}Zr_{0.1}Y_{0.1}O_{3-\delta}$ (x= 0.1, 0.2, 0.4, 0.6 and 0.7)

BCFZY powder was synthesized via the EDTA-citric acid complexing sol-gel route.[10] Stoichiometric amounts of $Ba(NO_3)_2$ (Alfa Aesar, 99 %), $Co(NO_3)_2 \bullet 6H_2O$ (Alfa Aesar, 98-102 %), $Fe(NO_3)_2 \bullet 9H_2O$ (Alfa Aesar, 98 %), $ZrO(NO_3)_2$ 35 wt.% in dilute nitric acid (Sigma Aldrich) and $Y(NO_3)_3 \bullet 6H_2O$ (Alfa Aesar, 99.9 %) were stirred in deionized water, with ethylenediaminetetraacetic acid (EDTA) and citric acid. The molar ratio of EDTA: citric acid: total metal ions was 1.5: 1.5: 1. Subsequently, ammonium hydroxide ($NH_3 \bullet H_2O$) was added to adjust the pH value to around 9 while heating the hot plate at 280 °C. Once a dark purple gel was formed, it was put into a drying oven at 150 °C for 24 h to dry completely. The resulting black charcoal was crushed with mortar and pestle, then pre-calcined at 600 °C for 5 h, followed by ball milling with isopropanol (IPA) and 3mm yttria-stabilized zirconia (YSZ) balls for 24 h. The powder was then dried in a heating oven at 90 °C.

2.2 Isotope exchange

For isotope exchange, sintered BCFZY pellets were prepared as explained in the supplementary information. Fig S1† shows that pure single-phase pellets were obtained for all BCFZY compositions after sintering. The oxygen isotope exchange was performed in a custom-built apparatus using a quartz tube mounted in a tube furnace. Pellets were first pre-annealed in a normal isotope $^{16}O_2$ atmosphere (21% $^{16}O_2$ + 79% N_2) at the same temperature with the annealing step. The isotope exchange was then carried out by annealing in an atmosphere of 99% enriched $^{18}O_2$ balanced with N_2 to maintain the same partial pressure of oxygen as in the pre-annealing step. A series of isotope exchange experiments were conducted for each BCFZY composition at temperatures ranging from 700 – 400 °C in 100° increments. The annealing time was an hour at 700 – 500 °C, and 24 h at 400 °C. The pre-annealing time was adjusted for each experiment to be long enough to ensure an equilibrium baseline defect concentration ($t_{\text{pre-anneal}} > 10t_{\text{anneal}}$).[21] In-line mass spectrometry was used to maintain an accurate concentration of isotope gas in the reactor. A rapid thermal quench was performed at the end of every pre-anneal and annealing processes by manual tilting of the reactor to remove the sample from the hot zone. After the isotope exchange process, the annealed samples were cross-sectioned and the two halves were mounted facing each other to minimize any sample distortions induced by the polishing step or the time-of-flight secondary ion mass spectrometry (ToF-SIMS) measurement. Lastly, the mounted samples were polished with successive grades of diamond spray down to a final polish of 0.05 μm.

2.3 ToF-SIMS measurement and data analysis

Before ToF-SIMS measurement, each sample was placed in vacuum overnight to remove water from the surface. Line-scanning was performed to determine the depth profile of the $^{16}O^-$ (m/z=16) and $^{18}O^-$ (m/z=18) using an ION-TOF instrument (TOF.SIMS 5, Germany). The profile of Y^+ and $^{94}Zr^+$ were also obtained to confirm that segregation of the B-site cations did not happen. Before each measurement, the surface of the sample was sputter-cleaned by using a 10 keV acceleration voltage, 10 nA total current Ar^{1200} cluster ion source in non-interlaced mode. The ToF-SIMS was operated using a liquid metal ion gun with a Bi+ ion source at 30 keV acceleration voltage and 2 pA total current in static mode. The sputter crater size was 700×700 μm², and the 500×500 μm² region at the center of the crater was analyzed. Charge compensation was achieved by an electron flood gun, and the extended dynamic range feature was applied for the case of $^{16}O^-$ saturation. The line-scanning data for oxygen ions was calculated in terms of isotope fraction $C(x)$, which was further corrected for the isotope fraction of the natural background C_{bg} (0.2 %) and the annealing gas C_g (99 %). The normalized isotope fraction $C'(x)$ was fitted with the diffusion solution in the semi-infinite medium, as shown in Equation 1.[22] Here, D^* is the tracer diffusion coefficient, k^* is the surface exchange of the tracer, x is the depth from the surface, t is the annealing time, and h is the k^*/D^* ratio, respectively. D^* and k^* were obtained by non-linear least-squares fitting of the solution equation (Equation 1).

with the MATLAB® curve fitting toolbox. The precision of fitting results was quantified with a 95% prediction interval.

$$C'(x) = \frac{C(x) - C_{\mathrm{bg}}}{C_{\mathrm{g}} - C_{\mathrm{bg}}} = \mathrm{erfc}\left(\frac{x}{2\sqrt{D^* t}}\right) - \exp(hx + h^2 D^* t) \times$$

$$\mathrm{erfc}\left\{\left(\frac{x}{2\sqrt{D^* t}}\right) + \left(h\sqrt{D^* t}\right)\right\} \quad (1)$$

2.4 The structure and microstructure characterization

The thermal expansion coefficient (TEC) of various BCFZY compositions was obtained by XRD analysis under air (step size: 0.0290 °, angular range: 20 – 120 °). The in-situ HT-XRD was carried out in the temperature range 35 to 800 °C with a heating rate of 5 °C·min^{-1} using an Empyrean XRD (Malvern Panalytical Ltd, UK) equipped with DHS1100 dome hot stage heating attachment (Anton Paar GmbH, Austria). An Anton Paar polyether ether ketone (PEEK) dome was used to maintain stable and accurate temperature and atmosphere. The X-ray patterns were acquired every 100 °C from 35 to 600 °C and every 50 °C from 600 to 800 °C. For each temperature step, the sample was held until equilibrium was reached prior to final measurement acquisition. Lastly, an X-ray pattern was obtained at 35 °C after cooling to confirm the lack of structural alteration/phase change. XRD (PANalytical, Netherlands) was measured mixture of Ni and $BaCe_{0.4}Zr_{0.4}Y_{0.1}Yb_{0.1}O_{3-\delta}$ (BCZYYb4411) at room temperature after sintering 1475 °C for 5 h to identify phase purity with Cu-Kα radiation tube voltage 45 kV, and tube current 40 mA. The data was collected in the 2 θ range from 20 to 80 ° with a step size of 0.008 ° and 5 sec at each step. The microstructure was investigated using Field Emission Scanning Electron Microscopy (FE-SEM, JEOL JSM-7000F).

2.5 Measurements of DC electrical conductivity

A DC 4-probe method was used to obtain the electrical conductivity of various BCFZY compositions in dry air (40 sccm) in a tube furnace. Dense sample pellets were prepared with the same method used for the tracer diffusion ToF-SIMS samples. Due to the relatively low electrical conductivity of BCFZY, silver paste electrodes were applied on the pellets to collect the current. The paste was cured at 700 °C for 5 h before the measurements. The conductivities were measured after reaching equilibrium at each temperature using a potentiostat in a 4-electrode configuration (Gamry interface 1010E, USA).

2.6 Full assembly cell testing

The full assembly cell was placed on an alumina tube and sealed using Cerambond (552-VFG). High purity hydrogen was used as fuel, with synthetic air (21% O_2 + 79% N_2) as oxidant gas. Water vapor was added to the synthetic air stream through a bubbler with 3 vol.% H_2O at room temperature. The cell was reduced at 600 °C under 5 vol.% H_2 and 95 vol.% N_2, before gradually increasing to 100 vol.% H_2 with a flow rate of 50 mL·min^{-1} at the anode. 300 mL·min^{-1} air was fed to the cathode during the reducing process of the cell, and all electrochemical testing, including I-V polarization and EIS was performed using a Gamry Reference 3000. The EIS measurements were performed at open circuit voltage using a signal amplitude of 10 mV in the frequency range of 10^6–10^{-1} Hz.

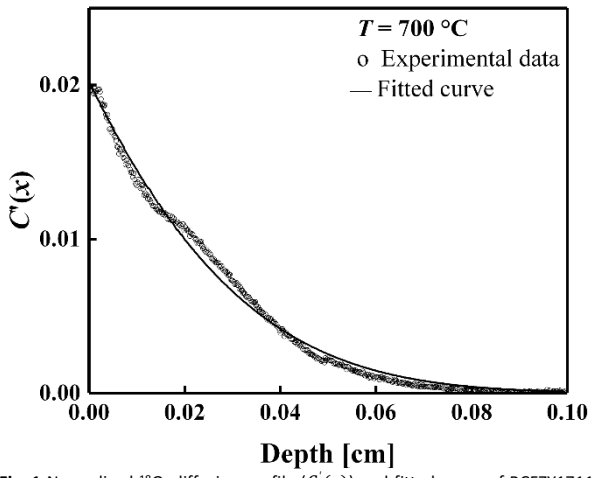

Fig. 1 Normalized ^{18}O diffusion profile ($C'(x)$) and fitted curve of BCFZY1711 exchanged at 700 °C for 2 h

2.7 Symmetric cell testing

Pt and Ag paste with silver wire were placed on the symmetric cell electrodes using the same method used for full button cell assembly. EIS measurement of the symmetric cells was conducted under 100 mL·min^{-1} of humidified synthetic air (3 vol.% H_2O) in the temperature range of 400 – 450 °C.

2.8 Faradaic efficiency measurement

Electrochemically produced hydrogen was measured at exhaust gas line of the fuel electrode under electrolysis operation. The gas chromatograph (GC, Agilent 3000 A) was used to detect electrochemically produced hydrogen and the exhaust volumetric flow rate was measured using a flow meter (DryCal Defender 530 Plus, Mesa Labs). The faradaic efficiency of the cell was calculated as the ratio of measured H_2 production to theoretical H_2 production.

3. Results and discussion

3.1 Oxygen tracer diffusion and surface exchange rate

In this work, we apply the isotope exchange technique to quantify oxygen ion incorporation and transport in the BCFZY system as a function of the Co/Fe ratio. Fig.1 shows an example of a typical normalized ^{18}O diffusion profile obtained by ToF-SIMS measurement from a dense BCFZY1711 sample. To ensure accuracy, six spots on each sample were investigated during each measurement and each sample was measured two times (for a total of 12 measurements per composition and condition); measurement variance was found to be extremely small (e.g., typically less than ±1%), suggesting excellent reproducibility for the SIMS measurement and subsequent fitting procedure. The resulting complete data set for the oxygen ion tracer diffusivity ($D^*_{O^{2-}}$) and surface exchange

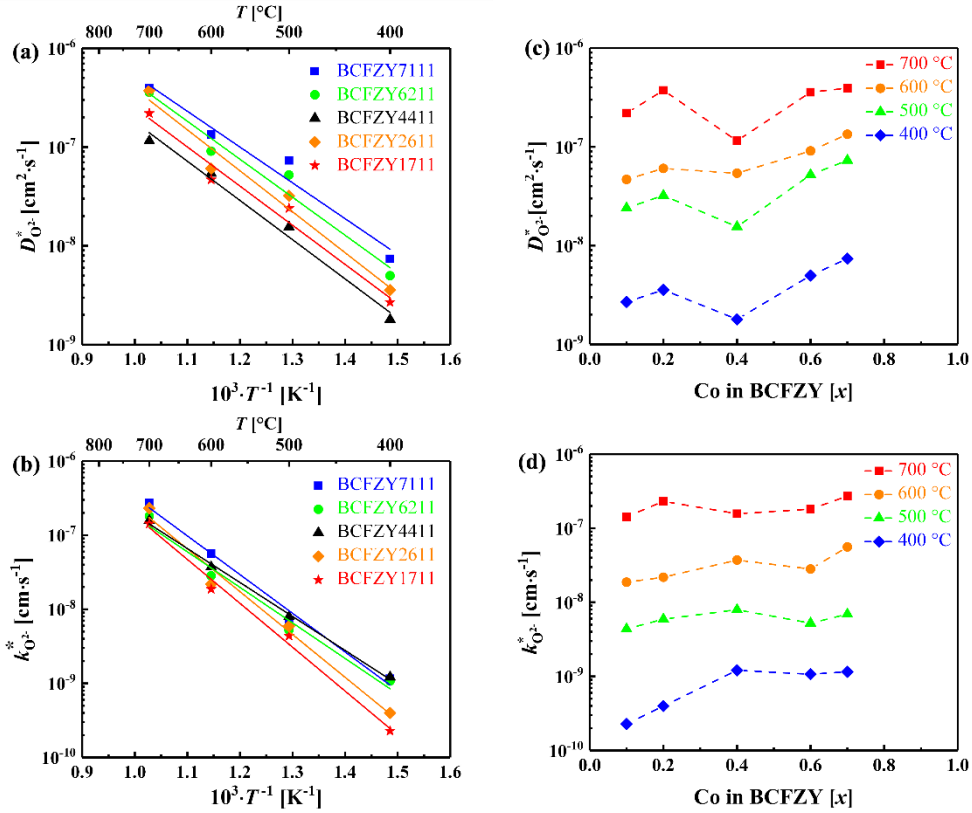

Fig. 2 a) Oxygen ion tracer diffusivities and b) surface exchange coefficients for various BCFZY compositions as a function of inverse temperature. Co/Fe ratio dependence of c) the oxygen ion tracer diffusivity and d) surface exchange rate. The solid lines in a and b are Arrhenius fits for activation energy estimation while the dashed lines in c and d are for visual guidance only. Each data point represents an average of at least 6 measured spots for each sample; in all cases, the error was smaller than the size of the symbols for both $D^*_{O^{2-}}$ and $k^*_{O^{2-}}$.

coefficient ($k^*_{O^{2-}}$) as a function of temperature and BCFZY composition is provided in Fig. 2. In all both $D^*_{O^{2-}}$ and $k^*_{O^{2-}}$, thus error cases, the uncertainty (95% confidence interval) was smaller than the size of the symbols for bars are not included in Fig. 2.

As shown in Fig. 2a,b, both $D^*_{O^{2-}}$ and $k^*_{O^{2-}}$ show clear Arrhenius temperature-activated behavior. While the oxygen tracer diffusion activation energy is essentially invariant with Co/Fe ratio (~69 – 79 kJ·mol^{-1}), the oxygen surface exchange activation energy generally decreases with increasing Co/Fe ratio and varies more widely (from ~113 kJ·mol^{-1} to ~87 kJ·mol^{-1})—see Table 1 and Fig. S2† (a) for details. Meanwhile, as shown in Fig. S2† (b), the pre-exponential factor for $D^*_{O^{2-}}$ ($D^\circ_{O^{2-}}$) does not show a distinct trend with Co composition and varies only modestly with composition. In contrast, the pre- surface exchange rates, especially at low temperatures. We can also observe in Fig. S3† that the values of $D^*_{O^{2-}}$ and $k^*_{O^{2-}}$ increase consistently as temperature increase, and that higher bulk diffusion generally correlates with faster surface kinetics, which is a commonly observed phenomenon across many mixed conducting oxide systems.[23] As shown in Fig. 2c,d, both $D^*_{O^{2-}}$ and $k^*_{O^{2-}}$ increase with increasing Co/Fe ratio. The compositional effect is strongest at lower temperatures (e.g., 400 °C), especially for $k^*_{O^{2-}}$. In other words, higher Co content appears to be particularly beneficial for low temperature performance. The higher Fe-O bond energy relative to Co-O is generally observed to result in higher energy barriers for both surface exchange and oxygen ion diffusion, which is consistent with our findings.[24,25] While the trends are generally quite consistent across compositions and temperatures, we note occasional variations. For example, the BCFZY6211 $k^*_{O^{2-}}$ values at 500 and 600 °C (Fig. 2d) trend slightly below the analogous values for BCFZY4411. These slight discrepancies likely reflect sample-to-sample variations in the surface roughness. Although diamond polishing was performed for all samples, we have noted that the surface roughness can vary based on the initial sample condition; it is believed that this discrepancy does not affect the data significantly; it does not impact the overall conclusion that D* and k* generally increase with increasing Co content, although this trend becomes less significant at higher

Table 1 Activation energies of oxygen ion tracer diffusivity and surface exchange coefficient for various BCFZY compositions.

Composition	$E_{a\,D^*}$ [kJ·mol^{-1}]	$E_{a\,k^*}$ [kJ·mol^{-1}]
BCFZY4411	76.03±11.0	87.71±2.5
BCFZY7111	69.37±9.3	99.96±6.9
BCFZY6211	73.62±9.9	91.76±9.4
BCFZY2611	79.41±10.4	110.96±10.3
BCFZY1711	75.84±8.3	112.89±7.3

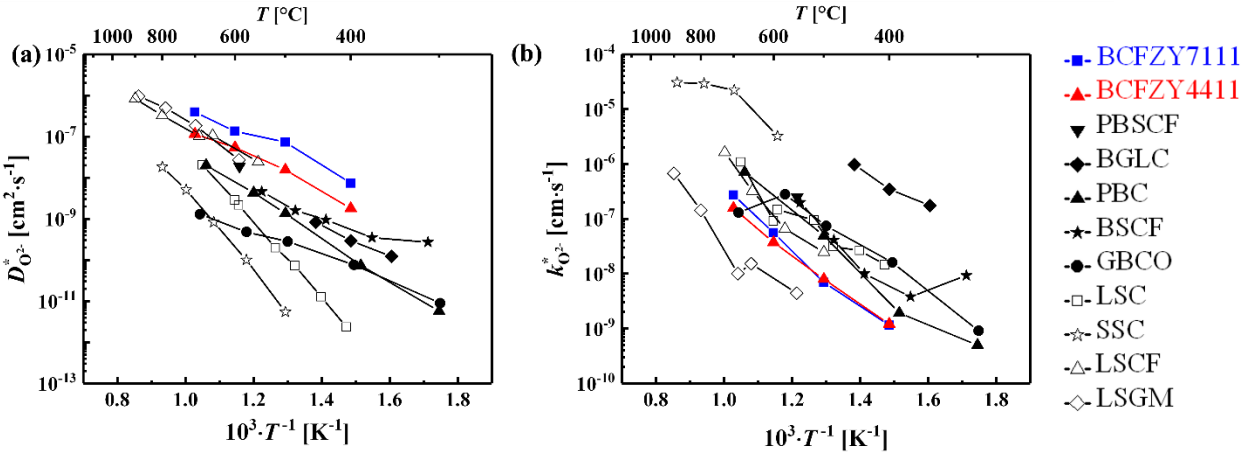

Fig. 3 Arrhenius plots of a) oxygen ion tracer diffusivity and b) surface exchange rate of various TCO and MIEC cathode materials: ▼$PrBa_{0.5}Sr_{0.5}Co_{1.5}Fe_{0.5}O_{5+\delta}$ (PBSCF)[69], ◆$Ba_{0.5}Gd_{0.8}La_{0.7}Co_2O_{6-\delta}$ (BGLC)[70], ▲$PrBaCo_2O_{5+\delta}$ (PBC)[71], ★$Ba_{0.5}Sr_{0.5}Co_{0.8}Fe_{0.2}O_{3-\delta}$ (BSCF)[72], ●$GdBaCo_2O_{5+\delta}$ (GBCO)[73], ■$La_{0.6}Sr_{0.4}CoO_{3-\delta}$ (LSC)[72], ☆$Sm_{0.4}Sr_{0.6}CoO_{3-\delta}$ (SSC)[74], △$La_{0.6}Sr_{0.4}Co_{0.2}Fe_{0.8}O_{3-\delta}$ (LSCF)[75], and ◇$La_{0.9}Sr_{0.1}Ga_{0.8}Mg_{0.2}O_{2.85}$ (LSGM)[76]. The solid lines are visual guidance.

temperatures. For example, at 700 °C, the Co-rich compositions show only slightly higher $D^*_{O^{2-}}$ and $k^*_{O^{2-}}$ values compared to the Fe-rich compositions. Interestingly, the $D^*_{O^{2-}}$ values for BCFZY4411 (Fig. 2c) deviate notably from the general trend, as this composition exhibits the lowest bulk diffusion at all temperatures. It has been reported that a compositionally uniform arrangement of B-site cations facilitates enhanced migration pathways for mobile ionic charge carriers with fewer trap sites.[26] Gazda et al. and Chroneos et al. also found that the cation distribution in oxygen ion-conducting oxides influences the energy barriers for migration entropy, bonding length, elastic strain, and in consequence, oxygen transport.[27,28] We speculate that BCFZY4411 presents the greatest B-site cation disorder as it has an equimolar Co/Fe content ratio of 1:1, thereby causing a maximally frustrated energy landscape for oxygen migration in the bulk. We note that in contrast to $D^*_{O^{2-}}$, the $k^*_{O^{2-}}$ is not impacted significantly by the cation arrangement (Fig. 2d) and tends to increase with increasing cobalt content without a deviation for the BCFZY4411 composition. This is consistent with the fact that the surface exchange rate depends primarily on overall electronic structure factors such as σ^*-orbital (e_g) occupation and average B-O bond covalency, as well as oxygen vacancy concentration, rather than the specific local arrangement or ordering of B-site cations[29,30].

In summary, the isotope exchange tracer diffusion studies demonstrate that the Co-rich BCFZY compositions possess the highest bulk diffusion and surface exchange kinetics, while the Fe-rich compositions generally show the lowest bulk diffusion and surface exchange kinetics; furthermore, the differences are most pronounced at lower temperatures. A complete archive of the isotope tracer diffusion data sets and fitted $D^*_{O^{2-}}$ and $k^*_{O^{2-}}$ values for the various BCFZY compositions under all conditions is provided for reference in the supplementary information.

Fig. 3 compares the kinetic parameters ($D^*_{O^{2-}}$ and $k^*_{O^{2-}}$) for the BCFZY7111 and BCFZY4411 compositions obtained in this work against other TCO and MIEC cathode materials. BCFZY7111 demonstrates the highest oxygen bulk diffusion performance amongst all reported cathode materials (Fig. 3a). It is notable that BCFZY4411 and BCFZY7111 both exhibit outstanding bulk diffusion even at low temperatures (≤ 500 °C). This result is consistent with the excellent fuel cell and electrolysis performance reported for BCFZY4411 in a variety of low-temperature protonic ceramic electrochemical devices, and suggests that BCFZY7111 may provide even higher performance.[10,31,32] It also suggests that BCFZY7111 may hold promise as an oxygen transport membrane. On the other hand, BCFZY4411 and BCFZY7111 exhibit relatively low surface exchange kinetics in comparison to other MIEC and TCO cathode materials (Fig. 3b). Thus, while bulk/surface diffusion is often the rate determining step (RDS) for many cathode materials, it is more likely that the surface exchange process can be rate-determining in BCFZY cathodes. This puts an emphasis on high-surface area nano structuring in BCFZY cathode design to overcome surface kinetic limitations. These findings also

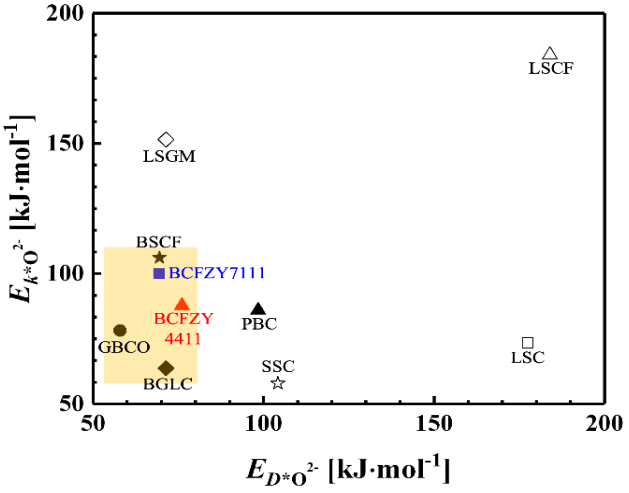

Fig. 4 Comparison plot of activation energies for oxygen ion tracer diffusivity and surface exchange coefficient of various TCO and MIEC cathode materials: ◆$Ba_{0.5}Gd_{0.8}La_{0.7}Co_2O_{6-\delta}$ (BGLC)[70], ▲$PrBaCo_2O_{5+\delta}$ (PBC)[71], ★$Ba_{0.5}Sr_{0.5}Co_{0.8}Fe_{0.2}O_{3-\delta}$ (BSCF)[72], ●$GdBaCo_2O_{5+\delta}$ (GBCO)[73], ■$La_{0.6}Sr_{0.4}CoO_{3-\delta}$ (LSC)[72], ☆$Sm_{0.4}Sr_{0.6}CoO_{3-\delta}$ (SSC)[74], △$La_{0.6}Sr_{0.4}Co_{0.2}Fe_{0.8}O_{3-\delta}$ (LSCF)[75], and ◇$La_{0.9}Sr_{0.1}Ga_{0.8}Mg_{0.2}O_{2.85}$ (LSGM)[76]. Yellow shade indicates the area of high-performance low temperature cathode materials.

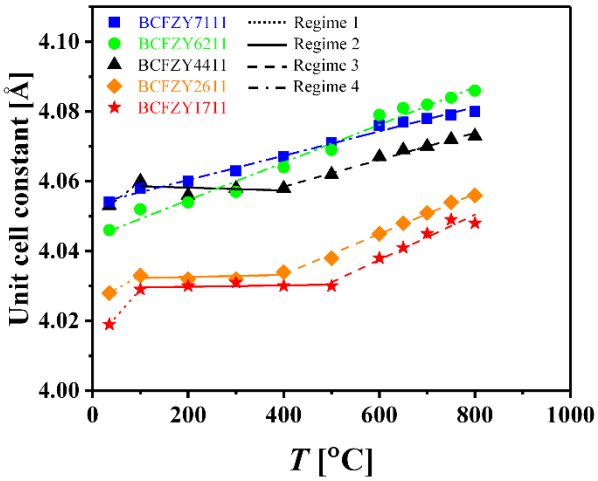

Fig. 5 Evolution of the lattice parameter for the various BCFZY compositions as a function of temperature. The dotted lines, solid lines, dashed lines, and dashed-dot lines are the fittings for regime 1, 2, 3, and 4 respectively.

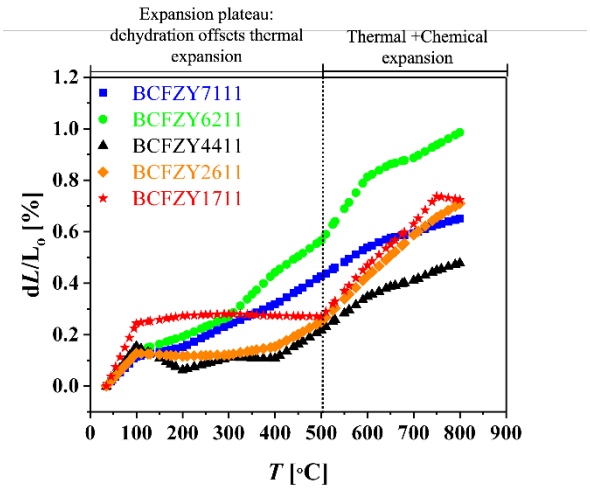

Fig. 6 Total expansion curves for various BCFZY compositions in the temperature range 35 – 800 °C. Dotted lines separate the low-T dehydration regime from the high-T thermal + chemical expansion regime.

suggest that a composite electrode strategy, where a BCFZY backbone is functionalized with nanoparticles of a second TCO or MIEC oxide possessing higher surface exchange kinetics may be a powerful method to further enhance electrochemical performance. Finally, it should be noted that the surface exchange process is not a direct measure of electrochemical activity as it reflects a purely chemical incorporation process in contrast to the voltage-activated charge transfer process associated with ORR or oxygen evolution reaction (OER) in an electrochemical cell; thus, caution should be exercised when evaluating potential electrode materials solely on the basis of their chemical surface exchange kinetics.

Fig. 4 compares the $E_{D^*_{O^{2-}}}$ and $E_{k^*_{O^{2-}}}$ values of various TCO and MIEC cathode materials, including BCFZY7111 and BCFZY44111. For low-temperature electrochemical applications, it is important to have low values for both $E_{D^*_{O^{2-}}}$ and $E_{k^*_{O^{2-}}}$ (i.e., the lower left-hand corner yellow-shaded region of the plot). Thus, $GdBaCo_2O_{5+\delta}$ (GBCO), $Ba_{0.5}Gd_{0.8}La_{0.7}Co_2O_{6-\delta}$ (BGLC), BCFZY, and $Ba_{0.5}Sr_{0.5}Co_{0.8}Fe_{0.2}O_{3-\delta}$ (BSCF) appear particularly attractive in this respect. Notably, all four of these cathode systems incorporate high concentrations of A-site Ba and B-site Co.

3.2 Structural characterization, thermal expansion, and DC electrical conductivity

In-situ HT-XRD analysis was performed to obtain the structure parameters and quantify the thermal expansion behaviour for all studied BCFZY compositions from 35 to 800 °C under dry air. The temperature-resolved diffraction patterns are summarized in Fig. S4† along with a pure SiC XRD pattern that was acquired for in-situ 2θ calibration. All BCFZY compositions were determined to be purely crystalline with the cubic perovskite structure (space group Pm-3m) and without detectable phase impurity. As shown in Fig. S4†, the characteristic reflections clearly shift towards lower angles during heating, consistent with an increase in unit cell constant. The unit cell parameters as a function of composition and temperature were calculated from the XRD data as shown in Fig. 5. First, we note that there is an increase in the room-temperature unit-cell constant with increasing Co-content up to BCFZY4411. However, at still higher Co content, the room-temperature unit cell constant decreases slightly. At room-temperature, the possible valence states for Co and Fe are +3 and +4, assuming that the Ba valence state is maintained as +2. Although Co and Fe are most stable as Co^{+3} and Fe^{+3} in perovskite structure, it is likely that a fraction of the Fe and/or Co exist in the +4 valence state to maintain electroneutrality when the oxygen lattice sites are not fully filled at room-temperature.[33,34] It is our hypothesis that at room-temperature, the valence state of Fe is +4, while the Co cations distribute between +3/+4 valance states, with the amount of Co in the +3 valance state (higher ionic radius) increasing with increasing Co content. Thus, the high Co content BCFZY compositions have higher unit cell parameters. The +4 oxidation state for Fe at room-temperature likely contributes to the high TEC behaviour of high Fe content BCFZY compositions. This will be discussed further later in this section.

We observe distinctly different thermal expansion behaviour for the Fe-rich and equimolar compositions (BCFZY1711, 2611, and 4411) as compared to the Co-rich compositions (BCFZY6211, 7111). For the Fe-rich and equimolar compositions, we observe three distinct thermal expansion regimes (Regimes 1, 2, and 3). After an initial linear thermal expansion response at low temperature (Regime 1), the thermal expansion response plateaus between ~100 °C and ~400 – 500 °C (Regime 2). Finally, linear thermal expansion resumes up to the terminal measurement temperature of 800 °C (Regime 3). The Co-rich BCFZY compositions, in contrast, exhibit a more conventional and nearly constant linear thermal expansion response across the entire measured temperature range (Regime 4), although their expansion response is slightly reduced in the ~100 – 300 °C temperature range.

The acute increase of unit cell parameter at Regime 1 may be due to a spin state transition. The spin state transition in Co is more flexible than Fe, thus it is possible that Co spin state

Table 2 Thermal expansion coefficients (TECs) of various BCFZY compositions at different temperature ranges determined by in-situ high temperature XRD analysis.

Temperature range	Thermal expansion coefficient [10^{-6} K^{-1}]				
	BCFZY7111	BCFZY6211	BCFZY4411	BCFZY2611	BCFZY1711
Regime 1	-	-	23.78	19.68	37.51
Regime 2	-	-	-1.57	-0.30	0.66
Regime 3	-	-	9.24	14.69	15.07
35 – 500 °C	9.17	12.15	4.69	5.37	5.82
500 – 800 °C	7.44	13.54	8.64	15.31	15.07

change affects the Regime 1 behaviour. Radovic et al. reported similar behaviour in $LaCoO_3$ where the Co changed from low to intermediate spin state at 25 – 230 °C.[35]

We attribute the thermal expansion plateau behaviour in the intermediate-temperature region to dehydration as described by Equation 2:

$$2OH_O^{\cdot} \leftrightarrow H_2O\,(g) + V_O^{\cdot\cdot} + O_O^{\times} \quad (2)$$

Dehydration causes a chemical contraction in proton-conducting oxides, which can offset thermal expansion and lead to plateau-like expansion behavior.[36–39] $BaFe_{0.6}Co_{0.3}Nb_{0.1}O_{3-\delta}$ and $BaCo_{0.7}Yb_{0.2}Bi_{0.1}O_{3-\delta}$, which are very similar Ba-containing Co and/or Fe-doped perovskite TCO materials, have been reported to show negative thermal expansion below 300 ℃ after intentional exposure to wet atmosphere and also upon exposure to ambient air at room temperature overnight due to water adsorption/desorption.[40] This finding demonstrates that water incorporation in Ba-containing perovskites can occur even at low temperatures and ambient humidity, which is in accordance with our hypothesis that the BCFZY samples were already hydrated under ambient air at room temperature before HT-XRD measurement, and therefore underwent dehydration during heating, leading to the TEC plateau behaviour. Depending on the basicity of dopant ions, the water

Table 3 Thermal expansion coefficients (TECs) of various electrolyte and cathode materials applied for PCFC.

Composition	Thermal expansion coefficient [10^{-6} K^{-1}]	Atmosphere	Temperature range [°C]	References
		Cathode		
BCFZY7111	8.51	Dry air	35 - 800	This work
BCFZY6211	12.73	Dry air	35 - 800	This work
BCFZY4411	23.78	Dry air	35 - 100	This work
	-1.57	Dry air	100 - 400	This work
	9.24	Dry air	400 - 800	This work
BCFZY2611	19.68	Dry air	35 - 100	This work
	-0.30	Dry air	100 - 400	This work
	14.69	Dry air	400 - 800	This work
BCFZY1711	37.51	Dry air	35 - 100	This work
	0.66	Dry air	100 - 500	This work
	15.07	Dry air	500 - 800	This work
LSGM	12.17	Dry air	30 - 1000	[43]
LSCF	17.5	Dry air	30 - 1000	[44]
		Electrolyte		
$BaZr_{0.8}Y_{0.2}O_{3-\delta}$ (BZY20)	8.2	Dry air	100 - 900	[37]
$BaZr_{0.9}Y_{0.1}O_{3-\delta}$ (BZY10)	13	Dry air	30 - 1000	[45]
	6.45	Moist air	27 - 375	[46]
	4.56	Moist air	375 - 500	[46]
$BaZ_{0.1}Ce_{0.7}Y_{0.2}O_{3-\delta}$	10.2	Dry air	50 - 900	[47]
$BaCe_{0.7}Zr_{0.1}Y_{0.1}Yb_{0.1}O_{3-\delta}$ (BCZYYb7111)	9.5	Dry air	RT - 1000	[48]
BCZYYb4411	9.8	Dry N_2	500 - 900	[49]

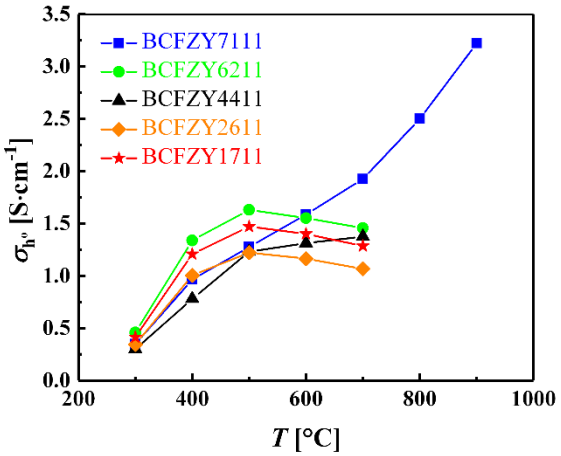

Fig. 7 DC electrical conductivities of various BCFZY compositions under dry air using a DC 4-probe method.

incorporation can vary; Waidha et al. found that the Co/Fe ratio significantly affects the water incorporation level, when Co and Fe are co-doped in similar perovskites.[41,42] Here, we observe that the plateau caused by dehydration decreases in extent and shifts to lower temperatures with increasing Co content. This is consistent with the studies cited above demonstrating that both the proton content and dehydration temperature in mixed Co/Fe-containing proton conducting oxides decreases with increasing Co content.[42] Moreover, the room-temperature unit cell parameters of the compositions measured after completing the entire HT-XRD heating cycle in dry air and cooling back to room temperature show a reduction of 0.1~0.5% compared to the initial values prior to heating (see details in Table S2†), with the equimolar and Fe-rich samples showing a larger degree of reduction. This shrinkage in the unit cell parameters is consistent with the dehydration that occurred during the heating process. While we strongly believe that chemical contraction due to dehydration is responsible for the plateau behaviour observed in these materials, further studies are warranted. Collecting temperature-resolved data during cool down to check for hysteresis or conducting additional in-situ XRD studies under wet air could provide additional insight. Furthermore, it is possible that other effects may also be influencing the intermediate-temperature expansion behaviour of these materials, such as orbital ordering change and second order phase transitions, as examined by Uhlenbruck et al. and/or interplay between competing $Fe^{3+}/^{4+}$ vs. $Co^{3+}/^{4+}$ valance and spin-state transitions coupled to changes in the oxygen vacancy concentration. [50–52]

Above the dehydration plateau, the expansion resumes. We attribute the high temperature expansion behaviour to a combination of thermal expansion and chemical expansion, where the chemical expansion component arises due to the creation of additional oxygen vacancies (Equation 2) coupled to reduction of the Fe and Co cations (denoted M in the Equation 3) as described by:

$$O_O^{\times} + 2h^{\cdot} \leftrightarrow \frac{1}{2}O_2(g) + V_O^{\cdot\cdot} \quad (2)$$

or

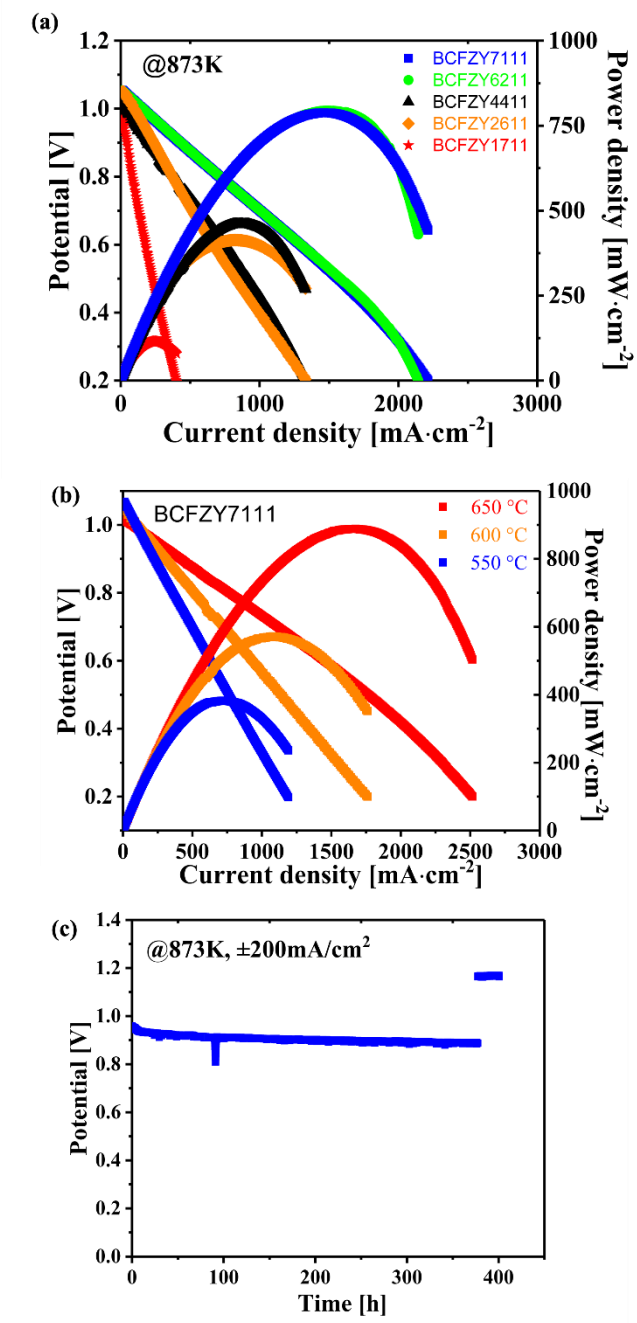

Fig. 8 (a) I-V-P curve of full cells using various BCFZY compositions as cathodes at 600 °C, (b) temperature dependence I-V-P curve of BCFZY7111 cathode on anode supported cell from 550 to 650 °C, and (c) stability test of BCFZY7111 under ±200 mA·cm^{-2} at 600 °C. The data were obtained under dry H_2 and humidified Air (3 vol.% H_2O and 20 % steam for electrolysis) for all measurements.

$$O_O^{\times} + 2M_M^{\cdot} \leftrightarrow \frac{1}{2}O_2(g) + V_O^{\cdot\cdot} + 2M_M^{\times} \quad (3)$$

The reduction process can be interpreted in terms of a consumption of localized p-type small polaron charge carriers (denoted in Equation 2 as $h^{\cdot}$) or a change in the redox state of the transition metal (TM) cations (Equation 3). The loss of lattice oxygen leads to a decrease in the average B-site cation (Co and Fe) valence states to maintain electroneutrality, resulting in an

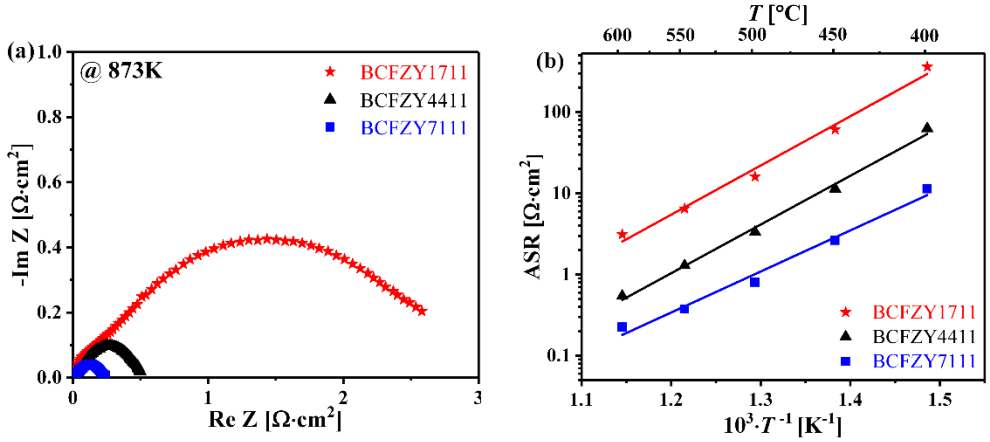

Fig. 9 Electrochemical performance of symmetric cells based on BCFZY1711, BCFZY4411 and BCFZY7111. a) Nyquist plot of BCFZY symmetric cells with varying Co content at 600 °C and b) temperature dependence of BCFZY symmetric cell ASR with varying Co content.

increase in the average B-site cation ionic radius and increase in coulombic repulsion near oxygen vacancies.[53] These two effects lead to chemical expansion, which acts in concert with thermal expansion in the high-temperature regime. Similar behaviour is observed in other Co and Fe- containing mixed conducting oxides including BSCF, PBSCF, and GBCO.[6,54–57] The thermal expansion behaviour observed here, combined with the oxygen tracer diffusion analyses, suggest that the mixed O^{2-}/H^{+} transport behaviour in the BCFZY TCO system can be tuned by tuning the Co/Fe ratio. We postulate that Fe-rich compositions favour enhanced hydration and protonic conduction at the expense of oxygen vacancy content and oxygen ion conductivity, while Co-rich compositions favour enhanced oxygen vacancy content and oxygen ion conductivity at the expense of protonic conduction. Total expansion curves (Fig. 6) were calculated from the unit cell constant vs. temperature data, from which TECs were estimated for each BCFZY composition in each distinct expansion regime (Table 2). As shown in the table, Fe-richBCFZY1711 exhibits the highest overall average TEC value (when averaged across the entire temperature range) while Co-rich BCFZY7111 shows the lowest overall TEC value when averaged across the entire temperature range. Considering just the high-temperature regime, where chemical and thermal expansion combine to dictate the overall expansion response (and dehydration should not influence behaviour), we again observe that the TEC roughly decreases with increasing Co content.

BCFZY4411 exhibits the lowest TEC at 35–500 °C and 500–800 °C. As mentioned earlier, the understanding of thermal expansion (Regime 2) is still not definitive; however, we assume that different Fe content leads the combinative effect on the oxygen vacancy concentration and Co-O bond length based on the suggested hypotheses in Fig. 5. At 500-800 °C, where the chemical and thermal expansions occur simultaneously, partial reduction of the Co oxidation state may ocurr.[33,58] Depending on the ratio of the Co oxidation state (+3 vs. +2), the radius change can vary. Increasing partial reduction can lead to an increase in average ionic radius. The Co^{+3} ions also can undergo a spin state transition in this temperature range. There are two possible spin-state for octahedrally-coordinated Co^{+3} at 500-800 °C, intermediate and high spin-state (IS and HS). If the spin-state changes from IS to HS, this can increase the ionic radius of Co^{+3}.[59–61]

Because the Co-rich BCFZY compositions likely already have a higher low-temperature oxygen vacancy content, they may experience less subsequent oxygen loss at high temperatures and hence less chemical expansion compared to the Fe-rich compositions. This would explain the greater expansion behaviour of the Fe-rich compositions in the high-temperature region. Plots combining the total expansion and TEC behaviour of each composition as a function of temperature are shown in Fig. S5†. Because Co-rich BCFZY7111 shows the lowest and most uniform TEC behaviour over the full 35-800 °C temperature range, we suggest that it should be particularly well suited for electrochemical cell application. The TEC properties of the various BCFZY compositions studied here are compared to other reported cathode materials as well as to common proton-conducting electrolyte materials in Table 3. As shown in the table, of all reported cathode materials, BCFZY7111 (TEC =8.5×10^{-6} K^{-1}) shows the closest TEC match to important common electrolyte materials such as BZY20 (TEC = 8.2×10^{-6} K^{-1}) and BCZYYb7111 (TEC = 9.5×10^{-6} K^{-1}). Intriguingly, BCFZY7111 shows an exceptionally low TEC for a Co-containing oxide, as most such oxides demonstrate high TECs in the range of 15 – 25×10^{-6} K^{-1} [44,62,63]. Fig. 7 shows the DC electrical conductivity of the various BCFZY compositions measured in dry air. With the exception of Co-rich BCFZY7111, electrical conductivity tends to peak/plateau at or above 500 °C at 1.25±0.5 $S\cdot cm^{-1}$. This behaviour is consistent with other known MIEC cathode materials such as BSCF and LSCF, although the absolute magnitude of the electrical conductivity observed in those other systems is generally higher.[19,20,44,64] Chen et al. reported that the loss of lattice oxygen with temperature (and the consequent increase in oxygen vacancies) consumes electron- holes and thus the electrical conductivity decreases after reaching a maximum.[19] Electrical conduction in these oxide systems is believed to occur via a temperature-activated small-polaron hopping process along the TM-O bond network. Thus, the competition between charge-carrier (polaron) mobility, which increases with temperature, and the charge-carrier concentration (which decreases with temperature) leads to this

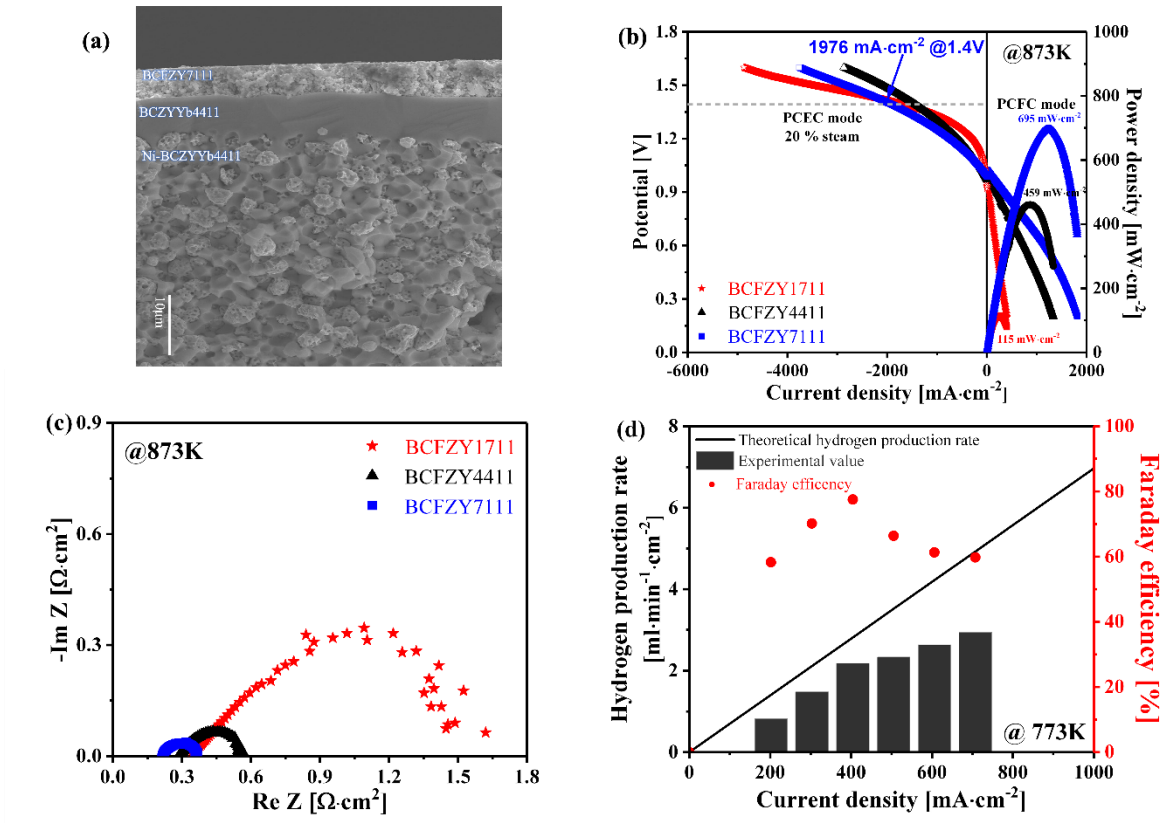

Fig. 10 Microstructure, fuel cell/electrolysis electrochemical performance, and electrolysis-mode Faradaic efficiency measurement of PCFC single cells prepared with varying BCFZY cathode composition. a) The FE-SEM cross sectional image of single cell with Ni-BCZYYb4411‖BCZYYb4411‖BCFZY7111 configuration; b) comparison of I-V and I-P curve for fuel cell mode and electrolysis mode at 600 °C for button cells of varying BCFZY cathode composition with the configuration Ni-BCZYYb4411‖BCZYYb4411‖BCFZYXXXX (XXXX =1711, 4411, and 7111). c) EIS Nyquist-format comparison for the same three cells at 600 °C under H_2/air at OCV; d) Faradic efficiency and hydrogen production rate as a function of the current density at 500 °C for a single button cell with BCFZY7111 cathode.

peak/plateau behaviour in the DC electrical conductivity response.

In contrast to the other compositions, however, the conductivity of Co-rich BCFZY7111 continues to increase with increasing temperature. We hypothesize that the greater covalency of the highly-percolated Co-O bond network in BCFZY7111 sufficiently increases the polaron mobility so as to overcome the loss of charge carriers at high temperatures, leading to a continued monotonic increase in electronic conductivity. Alternatively, the high Co content in BCFZY7111 may enable further partial reduction of the Co valence state above 500 °C from Co^{+3} to Co^{+2}, thereby facilitating an increase in the small-polaron charge carriers, and hence a continued increase in electrical conductivity with temperature. In simple oxides, the reduction Co valence state from trivalent to divalent is known to occur above 800 °C, while for Fe it occurs above 1560 °C, suggesting this theory is plausible.[33,58]

3.3 Symmetric and single cell tests

Based on the isotope tracer diffusion and thermomechanical studies discussed above, we hypothesize that Co-rich BCFZY7111 should be particularly promising for electrochemical cell application. To validate this hypothesis, we conducted full cell study using various BCFZY compositions as cathodes using an anode-supported cell architecture based on proton-conducting BCZYYb7111 electrolyte. As shown in Fig. 8a, the Co-rich BCFZY-based full cells (BCFZY7111 and 6211) performed the best while the Fe-rich BCFZY-based full cells showed the lowest performance at 600 °C, consistent with the results from the previous kinetic and thermomechanical studies. To study the temperature dependence of the electrochemical performance, a second BCFZY7111-based cell was fabricated and tested from 550-650 °C, the results of which are shown in Fig. 8b. As this cell had a somewhat thicker electrolyte, it produced slightly lower performance (see Fig. S8b† for direct comparison). However, this new BCFZY7111-based cell still exceeded the performance of the Fe-rich BCFZY-based cells and BCFZY4411, indicating that Co-rich BCFZY compositions produce higher PCFC performance. Finally, the durability of this cell was also tested for 377 hrs at a current density of 200 mA · cm^{-2} at 600 °C, showing a degradation rate of 2.5 %/100 hrs (Fig. 8c). The electrolysis mode was measured after fuel cell mode for 30 hrs at 200 mA · cm^{-2} at 600 °C with 0.3 %/100 hrs degradation rate.

For additional insight, we selected the highest Fe and Co content BCFZY (BCFZY1711 and BCFZY7111) and the equimolar BCFZY4411 compositions for further symmetric cell and full cell studies. First, EIS measurements were acquired from the three $BaCo_xFe_{0.8-x}Zr_{0.1}Y_{0.1}O_{3-\delta}$ ‖ BCZYYb7111 ‖ $BaCo_xFe_{0.8-x}Zr_{0.1}Y_{0.1}O_{3-\delta}$ symmetric cells to quantify the temperature dependence of the electrode ASR as a function of BCFZY composition under open

circuit voltage (OCV) conditions in air. Characteristic EIS spectra for the three BCFZY compositions at 600 °C are shown in Nyquist plot format in Fig. 9a. To facilitate direct comparison of the electrode polarization resistances, the high frequency ohmic electrolyte resistance has been subtracted from the spectra. Consistent with the isotope tracer diffusion studies, Co-rich BCFZY7111 shows the lowest electrode ASR, reaching 0.22 Ω·cm^2 at 600 °C, while Fe-rich BCFZY1711 shows the highest electrode ASR, 3.1 Ω·cm^2 at 600 °C. The temperature dependences of the electrode ASR for BCFZY7111, 4411, and 1711 are summarized in Arrhenius plot format in Fig. 9b. Electrode ASR decreases with increasing Co content at all temperatures. Furthermore, the activation energy associated with the electrode ASR also gradually decreases with increasing cobalt concentration from 1.2 eV for BCFZY1711 to 1 eV for BCFZY7111. This leads to greater outperformance for Co-rich BCFZY7111 vs. Fe-rich BCFZY1711 as the temperature is lowered (e.g., from ~14X at 600 °C to ~32X at 400 °C).

The electrochemical performance of BCFZY7111, 4411, and 1711 were assessed through single cell testing under both fuel cell and electrolysis mode operation. Further details on cell fabrication and testing are provided in the experimental methods section. A post-mortem scanning electron microscope (SEM) cross-sectional image of the BCFZY7111-based cell is shown in Fig. 10a. The porous anode substrate (Ni-BCZYYb4411) supports a thin dense electrolyte layer of BCZYYb4411 (7 – 8 μm) capped by a porous BCFZY7111 cathode layer (~5 – 6 μm thick). BCFZY1711 and BCFZY4411 cells were also prepared in the same manner and produced similar microstructures as shown in Fig. S6†. XRD (Fig. S7†) confirms the expected anode substrate and electrolyte phases, which were synthesized by solid state reactive sintering. The current-voltage (I-V) curves of all three cells under both fuel cell and electrolysis operation are shown in Fig. 10b. The cell based on the Co-rich BCFZY7111 cathode yields the highest fuel cell performance with a peak power density of 695 mW·cm^{-2} at 600 °C compared to 459 mW·cm^{-2} for BCFZY4411 and 115 mW·cm^{-2} for BCFZY1711. The performance of the BCFZY7111-based cell exceeds the value obtained for other modified BCFZY compositions measured under comparable conditions at 600 °C, including B0.9CFZY (668 mW·cm^{-2}) and BCFZY-0.95 (611 mW·cm^{-2}).[14,16] The performance of the BCFZY7111-based cell also compares favourably against several other reported MIEC cathodes including BSCF (622 mW·cm^{-2} @ 650 °C) and GBCO (146 mW·cm^{-2} @ 600 °C).[65,66]

Electrolysis mode performance was evaluated under 20% steam in air at 600 °C (fuel side sweep gas of H_2 50 sccm). At 1.4 V, the BCFZY7111, 4411, and 1711-based cells produced electrolysis-mode current densities of 1976, 1483, and 1783 mA·cm^{-2}. Interestingly, the performance of the Fe-rich BCFZY1711-based cell overtakes that of the Co-rich BCFZY7111-based cell at higher electrolysis voltages. This finding is consistent with recent reports that mixed Co/Fe oxides with high Fe content may offer enhanced OER performance compared to Co-rich compositions, although their fuel cell performance (ORR) is poorer.[67] High Fe content is hypothesized to reduce the oxidation state of Co and expand the potential range of thermodynamic metastability under electrolysis operating conditions.

In agreement with the I-V performance results, EIS spectra of the BCFZY7111, 4411, and 1711-based cells measured under OCV condition at 600 °C show a similar trend (Fig. 10c). Fig. S8a† shows the excellent reproducibility of the symmetric-cell EIS results using a second BCFZY7111-based symmetric cell, which produced results nearly identical to those provided in Fig. 10c after removing the electrolyte resistance. BCFZY7111 shows the lowest ohmic and polarization resistances of 0.217 and 0.15 Ω·cm^2 respectively, vs. 0.29 and 0.38 Ω·cm^2 for BCFZY4411, and 0.25 and 1.102 Ω·cm^2 for BCFZY1711. The hydrogen production rate was measured for the BCFZY7111 cell, from which faradaic efficiency (FE) was calculated as a function of current density at 500 °C as shown in Fig. 10d. The cell attains a peak FE of ~77 % at 400 mA·cm^{-2}, decreasing to ~59 % at 700 mA·cm^{-2}. These measured data are consistent with the well-known electronic leakage phenomenon in BCZYYb4411 which leads to relatively low FE, especially at low steam concentrations.[68]

4. Conclusions

In this work, we applied oxygen tracer diffusion and in-situ HT-XRD to study the oxygen ion incorporation/transport kinetics and thermomechanical behaviour of various BCFZY compositions to gain insight into the factors dictating electrochemical performance. We find that Co-rich compositions (e.g., BCFZY7111 and 6211) exhibit significantly higher bulk oxygen ion diffusion and surface exchange kinetics compared to Fe-rich compositions (e.g., BCFZY1711 and 2611). Furthermore, we identify anomalously low oxygen ion diffusion behaviour in the equimolar Co/Fe BCFZY4411 composition, which we attribute to the maximal B-site cation disorder presented by this composition. Co-rich BCFZY7111 demonstrates the highest oxygen ion bulk diffusivity so far reported among studied MIEC and TCO cathode materials, although its surface exchange kinetics are lower than many other reported materials. In-situ HT-XRD analysis reveals highly non-linear expansion behaviour in the Fe-rich BCFZY compositions which we ascribe to intermediate-temperature dehydration associated with a significant low-*T* proton concentration in these materials. The proton content of the Co-rich compositions is posited to be significantly lower, leading to a more uniform linear expansion behaviour. This finding, combined with the oxygen tracer diffusion experiments, suggest that the mixed O^{2-}/H^+ defect equilibria and transport behaviour in the BCFZY TCO system can be tuned by tuning the Co/Fe ratio. Finally, Co-rich BCFZY7111 shows the lowest and most uniform TEC behaviour over the full 35-800 °C temperature range (TEC = 8.5x10^{-6} K^{-1}), providing a good match to a number of common electrolyte materials including BZY20 and BCZYYb7111 and therefore reinforcing its potential for electrochemical cell application. This potential was verified by button cell testing, with the peak power density of a BCFZY7111-based cell reaching 695 mW·cm^{-2} at 600 °C in fuel cell mode (vs. 459 mW·cm^{-2} for BCFZY4411 and 115 mW·cm^{-2} for BCFZY1711), while the current density of the BCFZY7111-

based cell reaches 1976 mA·cm^{-2} @ 1.4 V (vs. 1483 mA·cm^{-2} for BCFZY4411 and 1783 mA·cm^{-2} for BCFZY1711) in electrolysis mode (also at 600 °C). Those results underscore the potential of Co-rich BCFZY as an ORR/OER electrode for intermediate-temperature fuel cell and electrolysis applications.

Author Contributions

Yewon Shin: investigation, visualization, analysis and interpretation of data, writing-original draft, editing, funding acquisition. You-dong Kim: investigation, visualization, writing-original draft. Michael Sanders: supervision, writing-review & editing. Steven P. Harvey: conceptualization, writing-review & editing. Ryan O'Hayre: project administration, conceptualization, analysis and interpretation of data, funding acquisition, writing-review & editing.

Conflicts of interest

There are no conflicts to declare.

Acknowledgements

The authors gratefully acknowledge CoorsTek, Inc for supporting this work through the CoorsTek Graduate Fellowship Program. This work was also supported by the Army Research Office under grant number W911NF-17-1-0051. Some SIMS experiments were acquired at the National renewable energy laboratory (NREL) in Golden. This work was authored in part by the National Renewable Energy Laboratory, operated by Alliance for Sustainable Energy, LLC, for the U.S. Department of Energy (DOE) under Contract No. DE-AC36-08GO28308. The views expressed in the article do not necessarily represent the views of the DOE or the U.S. Government. The U.S. Government retains and the publisher, by accepting the article for publication, acknowledges that the U.S. Government retains a nonexclusive, paid-up, irrevocable, worldwide license to publish or reproduce the published form of this work, or allow others to do so, for U.S. Government purposes. This material makes use of the TOF-SIMS system at the Colorado School of Mines (CSM), which was supported by the National Science Foundation under Grant No.1726898. All in-situ HT-XRD measurements were performed at the CSM Shared Facility. The authors also would like to thank Dr. Kenneth Steirer and Jake Huang for assistance for in-situ HT-XRD measurements and DC conductivity tests, respectively.

Notes and references

1. Samat AA, Darus M, Osman N, Baharuddin NA, Anwar M. A short review on triple conducting oxide cathode materials for proton conducting solid oxide fuel cell. In: AIP Conference Proceedings. 2021. p. 20233.
2. Papac M, Stevanović V, Zakutayev A, O'Hayre R. Triple ionic–electronic conducting oxides for next-generation electrochemical devices. Nat Mater. 2021;20(3):301–13.
3. Ding H, Wu W, Jiang C, Ding Y, Bian W, Hu B, et al. Self-sustainable protonic ceramic electrochemical cells using a triple conducting electrode for hydrogen and power production. Nat Commun. 2020;11(1).
4. Ryu S, Lee S, Jeong W, Pandiyan A, Krishna Moorthy SB, Chang I, et al. Pulsed laser deposition of BaCo0.4Fe0.4Zr0.1Y0.1O3-δ cathode for solid oxide fuel cells. Surf Coatings Technol. 2019 Jul;369:265–8.
5. Park S, Choi S, Shin J, Kim G. A collaborative study of sintering and composite effects for a PrBa0.5Sr0.5Co1.5Fe0.5O5+δ IT-SOFC cathode. RSC Adv. 2013 Dec 2;4(4):1775–81.
6. Zan J, Wang S, Zheng D, Li F, Chen W, Pei Q, et al. Characterization and functional application of PrBa0.5Sr0.5Co1.5Fe0.5O5+δ cathode material for IT-SOFC. Mater Res Bull. 2021 May 1;137:111173.
7. Wang W, Zhang X, Zhang D, Zeng Q, Jiang Y, Lin B. Highly promoted performance of triple-conducting cathode for YSZ-based SOFC via fluorine anion doping. Ceram Int. 2020 Oct 15;46(15):23964–71.
8. Duan C, Hook D, Chen Y, Tong J, O'Hayre R. Zr and Y co-doped perovskite as a stable, high performance cathode for solid oxide fuel cells operating below 500°C. Energy Environ Sci. 2017;10(1):176–82.
9. Li X, He L, Zhong X, Zhang J, Luo S, Yi W, et al. Evaluation of A-site Ba 2+ -deficient Ba 1−x Co 0.4 Fe 0.4 Zr 0.1 Y 0.1 O 3−δ oxides as electrocatalysts for efficient hydrogen evolution reaction. Scanning. 2018;2018.
10. Duan C, Tong J, Shang M, Nikodemski S, Sanders M, Ricote S, et al. Readily processed protonic ceramic fuel cells with high performance at low temperatures. Science (80-). 2015;349(6254):1321–6.
11. Choi S, Kucharczyk CJ, Liang Y, Zhang X, Takeuchi I, Ji H Il, et al. Exceptional power density and stability at intermediate temperatures in protonic ceramic fuel cells. Nat Energy. 2018;3(3):202–10.
12. Strandbakke R, Cherepanov VA, Zuev AY, Tsvetkov DS, Argirusis C, Sourkouni G, et al. Gd- and Pr-based double perovskite cobaltites as oxygen electrodes for proton ceramic fuel cells and electrolyser cells. Solid State Ionics. 2015 Oct 1;278:120–32.
13. Wang W, Zhang X, Khan K, Wu H, Zhang D, Yang Y, et al. Enhanced ORR activity of A-site deficiency engineered BaCo0·4Fe0·4Zr0·1Y0·1O3-δ cathode in practical YSZ fuel cells. Int J Hydrogen Energy. 2021;46(7):5593–603.
14. Ren R, Wang Z, Xu C, Sun W, Qiao J, Rooney DW, et al. Tuning the defects of the triple conducting oxide BaCo0.4Fe0.4Zr0.1Y0.1O3-: δ perovskite toward enhanced cathode activity of protonic ceramic fuel cells. J Mater Chem A. 2019;7(31):18365–72.
15. Kuai X, Yang G, Chen Y, Sun H, Dai J, Song Y, et al. Boosting the Activity of BaCo0.4Fe0.4Zr0.1Y0.1O3−δ Perovskite for Oxygen Reduction Reactions at Low-to-Intermediate Temperatures through Tuning B-Site Cation Deficiency. Adv Energy Mater. 2019 Oct 1;9(38):1902384.
16. He F, Liang M, Wang W, Ran R, Yang G, Zhou W, et al. High-Performance Proton-Conducting Fuel Cell with B-Site-

Deficient Perovskites for All Cell Components. Energy and Fuels. 2020;34(9):11464–71.
17. Duffy JH, Meng Y, Abernathy HW, Brinkman KS. Surface and bulk oxygen kinetics of baco0.4fe0.4zr0.2−xyxo3−δ triple conducting electrode materials. Membranes (Basel). 2021;11(10).
18. Papac MC, Talley KR, O'Hayre R, Zakutayev A. Instrument for spatially resolved, temperature-dependent electrochemical impedance spectroscopy of thin films under locally controlled atmosphere. Rev Sci Instrum. 2021 Jun 3;92(6):065105.
19. Chen Z, Ran R, Zhou W, Shao Z, Liu S. Assessment of Ba0.5Sr0.5Co1-yFeyO3-δ (y = 0.0-1.0) for prospective application as cathode for IT-SOFCs or oxygen permeating membrane. Electrochim Acta. 2007 Sep;52(25):7343–51.
20. Tai LW, Nasrallah MM, Anderson HU, Sparlin DM, Sehlin SR. Structure and electrical properties of La1-xSrxCo1-yFeyO3. Part 1. The system La0.8Sr0.2Co1-yFeyO3. Solid State Ionics. 1995 Mar 1;76(3–4):259–71.
21. De Souza RA, Chater RJ. Oxygen exchange and diffusion measurements: The importance of extracting the correct initial and boundary conditions. Solid State Ionics. 2005;176(23–24):1915–20.
22. Crank J. The mathematics of diffusion. Vol. 5, Oxford University Press. 1975. 36 p.
23. De Souza R., Kilner J. Oxygen transport in La1−xSrxMn1−yCoyO3±δ perovskites Part II. Oxygen surface exchange. Solid State Ionics. 1999;126(1–2):153–61.
24. Lee KT, Manthiram A. Characterization of Nd0.6Sr0.4Co1-yFe yO3-δ (0 ≤ y ≤ 0.5) cathode materials for intermediate temperature solid oxide fuel cells. Solid State Ionics. 2005 May 31;176(17–18):1521–7.
25. Lv H, Zhao BY, Wu YJ, Sun G, Chen G, Hu KA. Effect of B-site doping on Sm0.5Sr0.5MxCo1-xO3-δ properties for IT-SOFC cathode material (M = Fe, Mn). Mater Res Bull. 2007 Dec 4;42(12):1999–2012.
26. Shen L, Du Z, Zhang Y, Dong X, Zhao H. Medium-Entropy perovskites Sr(FeαTiβCoγMnζ)O3-δ as promising cathodes for intermediate temperature solid oxide fuel cell. Appl Catal B Environ. 2021 Oct 15;295.
27. Gazda M, Miruszewski T, Jaworski D, Mielewczyk-Gryń A, Skubida W, Wachowski S, et al. Novel Class of Proton Conducting Materials - High Entropy Oxides. ACS Mater Lett. 2020;2(10):1315–21.
28. Chroneos A, Yildiz B, Tarancón A, Parfitt D, Kilner JA. Oxygen diffusion in solid oxide fuel cell cathode and electrolyte materials: Mechanistic insights from atomistic simulations. Energy Environ Sci. 2011;4(8):2774–89.
29. Wang L, Merkle R, Mastrikov YA, Kotomin EA, Maier J. Oxygen exchange kinetics on solid oxide fuel cell cathode materials-general trends and their mechanistic interpretation. J Mater Res. 2012;27(15):2000–8.
30. Suntivich J, Gasteiger HA, Yabuuchi N, Nakanishi H, Goodenough JB, Shao-Horn Y. Design principles for oxygen-reduction activity on perovskite oxide catalysts for fuel cells and metal-air batteries. Nat Chem. 2011;3(7):546–50.
31. Zhu L, O'Hayre R, Sullivan NP. High performance tubular protonic ceramic fuel cells via highly-scalable extrusion process. Int J Hydrogen Energy. 2021 Aug 5;46(54):27784–92.
32. Duan C, Kee R, Zhu H, Sullivan N, Zhu L, Bian L, et al. Highly efficient reversible protonic ceramic electrochemical cells for power generation and fuel production. Nat Energy. 2019;4(3):230–40.
33. Shao Z, Xiong G, Tong J, Dong H, Yang W. Ba effect in doped Sr(Co0.8Fe0.2)O3-d on the phase structure and oxygen permeation properties of the dense ceramic membranes. Sep Purif Technol. 2001 Oct 1;25(1–3):419–29.
34. Yokokawa H, Sakai N, Kawada T, Dokiya M. Thermodynamic stabilities of perovskite oxides for electrodes and other electrochemical materials. Solid State Ionics. 1992 May 1;52(1–3):43–56.
35. Radovic M, Speakman SA, Allard LF, Payzant EA, Lara-Curzio E, Kriven WM, et al. Thermal, mechanical and phase stability of LaCoO3 in reducing and oxidizing environments. J Power Sources. 2008 Sep 15;184(1):77–83.
36. Chen T, Jing Y, Anderson LO, Leonard K, Matsumoto H, Aluru N, et al. Toward Durable Protonic Ceramic Cells: Hydration-Induced Chemical Expansion Correlates with Symmetry in the Y-Doped BaZrO3-BaCeO3Solid Solution. J Phys Chem C. 2021;125(47):26216–28.
37. Andersson AKE, Selbach SM, Knee CS, Grande T. Chemical expansion due to hydration of proton-conducting perovskite oxide ceramics. J Am Ceram Soc. 2014;97(8):2654–61.
38. Mather GC, Muñoz-Gil D, Zamudio-García J, Porras-Vázquez JM, Marrero-López D, Pérez-Coll D. Perspectives on cathodes for protonic ceramic fuel cells. Vol. 11, Applied Sciences (Switzerland). 2021. p. 5324–34.
39. Sažinas R, Einarsrud MA, Grande T. Toughening of Y-doped BaZrO3 proton conducting electrolytes by hydration. J Mater Chem A. 2017;5(12):5846–57.
40. Majewski AJ, Slater PR, Steinberger-Wilckens R. Understanding the effect of water transport on the thermal expansion properties of the perovskites BaFe0.6Co0.3Nb0.1O3−δ and BaCo0.7Yb0.2Bi0.1O3−δ. J Mater Sci. 2020;55(28):13590–604.
41. Waidha AI, Ni L, Ali J, Lepple M, Donzelli M, Dasgupta S, et al. Synthesis of bifunctional BaFe 1Àx Co x O 3ÀyÀd (OH) y catalysts for the oxygen reduction reaction and oxygen evolution reaction †. 2020;
42. Zohourian R, Merkle R, Raimondi G, Maier J. Mixed-Conducting Perovskites as Cathode Materials for Protonic Ceramic Fuel Cells: Understanding the Trends in Proton Uptake. Adv Funct Mater. 2018 Aug 29;28(35).
43. Xue J, Shen Y, Zhou Q, He T, Han Y. Combustion synthesis and properties of highly phase-pure perovskite electrolyte Co-doped La0.9Sr0.1Ga0.8Mg0.2O2.85 for IT-SOFCs. Int J Hydrogen Energy. 2010 Jan 1;35(1):294–300.
44. Petric A, Huang P, Tietz F. Evaluation of La-Sr-Co-Fe-O perovskites for solid oxide fuel cells and gas separation membranes. Solid State Ionics. 2000 Nov 1;135(1–4):719–

25.
45. Goupil G, Delahaye T, Gauthier G, Sala B, Joud FL. Stability study of possible air electrode materials for proton conducting electrochemical cells. Solid State Ionics. 2012 Feb 23;209–210:36–42.
46. Braun A, Ovalle A, Pomjakushin V, Cervellino A, Erat S, Stolte WC, et al. Yttrium and hydrogen superstructure and correlation of lattice expansion and proton conductivity in the BaZr0.9 Y0.1 O 2.95 proton conductor. Appl Phys Lett. 2009;95(22).
47. Yang L, Liu Z, Wang S, Choi YM, Zuo C, Liu M. A mixed proton, oxygen ion, and electron conducting cathode for SOFCs based on oxide proton conductors. J Power Sources. 2010 Jan 15;195(2):471–4.
48. Zhang L, Yang S, Zhang S, Yang Y. Cerium and Gadolinium co-doped perovskite oxide for a protonic ceramic fuel cell cathode. Int J Hydrogen Energy. 2019 Oct 22;44(51):27921–9.
49. Nomura K, Shimada H, Yamaguchi Y, Shin W, Okuyama Y, Mizutani Y. Effect of Ce/Zr Ratio on Thermal and Chemical Expansions and CO 2 Resistance of Rare Earth-Doped Ba(Ce,Zr)O 3 Perovskite-Type Proton Conductors. ECS Meet Abstr. 2021 Jul 9;MA2021-03(1):93–93.
50. Uhlenbruck S, Tietz F. High-temperature thermal expansion and conductivity of cobaltites: Potentials for adaptation of the thermal expansion to the demands for solid oxide fuel cells. Mater Sci Eng B Solid-State Mater Adv Technol. 2004 Mar 25;107(3):277–82.
51. Yaremchenko AA, Kharton V V., Shaula AL, Patrakeev M V., Marques FMB. Transport properties and thermal expansion of perovskite-like La0.3Sr0.7Fe(Al,Cr)O3-δ ceramics. J Eur Ceram Soc. 2005;25(12 SPEC. ISS.):2603–7.
52. Kan WH, Lai KY, Huq A, Manthiram A. Unravelling the low thermal expansion coefficient of cation-substituted YBaCo4O7+δ. J Power Sources. 2016 Mar 1;307:454–61.
53. Armstrong TR, Stevenson JW, Pederson LR, Raney PE. Dimensional Instability of Doped Lanthanum Chromite. J Electrochem Soc. 1996;143(9):2919–25.
54. Kriegel R, Kircheisen R, Töpfer J. Oxygen stoichiometry and expansion behavior of Ba0.5Sr0.5Co0.8Fe0.2O3 - δ. Solid State Ionics. 2010 Feb 8;181(1–2):64–70.
55. McIntosh S, Vente JF, Haije WG, Blank DHA, Bouwmeester HJM. Oxygen stoichiometry and chemical expansion of Ba 0.5Sr 0.5Co 0.8Fe 4O 3-δ- measured by in situ neutron diffraction. Chem Mater. 2006 Apr 18;18(8):2187–93.
56. Choi M-B, Jeon S-Y, Im H-N, Wachsman ED, Song S-J. Oxygen Exchange Kinetics and Ionic Conductivity from Chemical Expansion Relaxation of Mixed Conducting Ba 0.5 Sr 0.5 Co 0.8 Fe 0.2 O 3-δ . J Electrochem Soc. 2011;159(2):P23–8.
57. Li N, Wei B, Lü Z, Huang X, Su W. GdBaCo2O5+δ-Sm0.2Ce 0.8O1.9 composite cathodes for intermediate temperature SOFCs. J Alloys Compd. 2011 Feb 24;509(8):3651–5.
58. Wei B, Lü Z, Huang X, Miao J, Sha X, Xin X, et al. Crystal structure, thermal expansion and electrical conductivity of perovskite oxides BaxSr1-xCo0.8Fe0.2O3- δ (0.3 ≤ x ≤ 0.7). J Eur Ceram Soc. 2006;26(13):2827–32.
59. Knížek K, Jirák Z, Hejtmánek J, Novák P, Ku W. GGA+U calculations of correlated spin excitations in LaCoO3. Phys Rev B - Condens Matter Mater Phys. 2009;79(1).
60. Knížek K, Jirák Z, Hejtmánek J, Veverka M, Maryško M, Maris G, et al. Structural anomalies associated with the electronic and spin transitions in LnCoO3. Eur Phys J B. 2005;47(2):213–20.
61. Araki W, Arai Y, Malzbender J. Transitions of Ba0.5Sr0.5Co0.8Fe 0.2O3-δ and La0.58Sr0.4Co 0.2Fe0.8O3-δ. Mater Lett. 2014 Oct 1;132:295–7.
62. Li M, Chen K, Hua B, Luo J li, Rickard WDA, Li J, et al. Smart utilization of cobaltite-based double perovskite cathodes on barrier-layer-free zirconia electrolyte of solid oxide fuel cells. J Mater Chem A. 2016 Dec 6;4(48):19019–25.
63. Lee JI, Park KY, Park H, Bae H, Saqib M, Park K, et al. Triple perovskite structured Nd1.5Ba1.5CoFeMnO9−δ oxygen electrode materials for highly efficient and stable reversible protonic ceramic cells. J Power Sources. 2021 Oct 31;510:230409.
64. Jung J Il, Misture ST, Edwards DD. Oxygen stoichiometry, electrical conductivity, and thermopower measurements of BSCF (Ba0.5Sr0.5CoxFe1-XO3-δ, 0≤ x ≤ 0.8) in air. Solid State Ionics. 2010 Sep 6;181(27–28):1287–93.
65. Zhou C, Sunarso J, Song Y, Dai J, Zhang J, Gu B, et al. New reduced-temperature ceramic fuel cells with dual-ion conducting electrolyte and triple-conducting double perovskite cathode. J Mater Chem A. 2019;7(21):13265–74.
66. Lin B, Zhang S, Zhang L, Bi L, Ding H, Liu X, et al. Prontonic ceramic membrane fuel cells with layered GdBaCo2O5+x cathode prepared by gel-casting and suspension spray. J Power Sources. 2008 Mar 1;177(2):330–3.
67. Kim BJ, Fabbri E, Abbott DF, Cheng X, Clark AH, Nachtegaal M, et al. Functional Role of Fe-Doping in Co-Based Perovskite Oxide Catalysts for Oxygen Evolution Reaction. J Am Chem Soc. 2019;141(13):5231–40.
68. Choi S, Davenport TC, Haile SM. Protonic ceramic electrochemical cells for hydrogen production and electricity generation: Exceptional reversibility, stability, and demonstrated faradaic efficiency. Energy Environ Sci. 2019;12(1):206–15.
69. Seong A, Kim J, Jeong D, Sengodan S, Liu M, Choi S, et al. Electrokinetic Proton Transport in Triple (H+/O2−/e−) Conducting Oxides as a Key Descriptor for Highly Efficient Protonic Ceramic Fuel Cells. Adv Sci. 2021;8(11).
70. Prato Modestino RA. TRANSPORT PROPERTIES AND SURFACE KINETICS OF Ba0.8+xGd0.8La0.2+xCo2O6−d. Ph.D thesis. 2016.
71. Burriel M, Peña-Martínez J, Chater RJ, Fearn S, Berenov A V, Skinner SJ, et al. Anisotropic oxygen ion diffusion in layered PrBaCo 2O 5+δ. Chem Mater. 2012;24(3):613–21.
72. Berenov A V, Atkinson A, Kilner JA, Bucher E, Sitte W. Oxygen tracer diffusion and surface exchange kinetics in La 0.6Sr0.4CoO3 - δ. Solid State Ionics. 2010;181(17–18):819–26.
73. Tarancón A, Skinner SJ, Chater RJ, Hernández-Ramírez F, Kilner JA. Layered perovskites as promising cathodes for

intermediate temperature solid oxide fuel cells. J Mater Chem. 2007;17(30):3175–81.

74. Fullarton IC, Jacobs JP, van Benthem HE, Kilner JA, Brongersma HH, Scanlon PJ, et al. Study of oxygen ion transport in acceptor doped samarium cobalt oxide. Ionics (Kiel). 1995;1(1):51–8.

75. Lane JA, Benson SJ, Waller D, Kilner JA. Oxygen transport in La0.6Sr0.4Co0.2Fe0.8O3-δ. Solid State Ionics. 1999;121(1):201–8.

76. Ishihara T, Kilner JA, Honda M, Sakai N, Yokokawa H, Takita Y. Oxygen surface exchange and diffusion in LaGaO3 based perovskite type oxides. Solid State Ionics. 1998;113–115:593–600.